Enhanced CO_2-to-CH_4 conversion via grain boundary oxidation effect in CuAg systems

Lei Wang [a,1], Xue Yao [b,1], Yi Xiao [a], Cheng Du [a], Xiyang Wang [a], Dmitry Akhmetzyanov [c,d], Zuolong Chen [a], Youchao Teng [a], Tao Guo [a], Yongzan Zhou [a], Joel P. Mills [a], Ning Chen [e], Weifeng Chen [e], Brant Billinghurst [e], Khaled M. Ibrahim [f], Jamie H. Warner [f], Chandra Veer Singh [b,g,*], Zhongchao Tan [a,h,**], Samira Siahrostami [i], Yimin A. Wu [a,c,**]

[a] Department of Mechanical and Mechatronics Engineering, University of Waterloo, Waterloo, Ontario N2L 3G1, Canada
[b] Department of Materials Science and Engineering, University of Toronto, Toronto, Ontario M5S 3E4, Canada
[c] Department of Chemistry, University of Waterloo, Waterloo, Ontario N2L 3G1, Canada
[d] Institute for Quantum Computing, University of Waterloo, Waterloo, Ontario N2L 3G1, Canada
[e] Canadian Light Source, Saskatoon, SK S7N 2V3, Canada
[f] Walker Department of Mechanical Engineering, the University of Texas of Austin, 204E. Dean Keeton St, Austin, TX 78712-1591, USA
[g] Department of Mechanical and Industrial Engineering, University of Toronto, Toronto, Ontario M5S 3G8, Canada
[h] Eastern Institute of Technology, No. 568 Tongxin Road, Zhenhai District, Ningbo, Zhejiang 315200, China
[i] Department of Chemistry, Simon Fraser University, 8888 University Drive, Burnaby, British Columbia V5A 1S6, Canada

ARTICLE INFO

ABSTRACT

The authentic active sites of oxide-derived copper (OD-Cu), namely grain boundaries (GBs) and oxidized $Cu^{\delta+}$ species, is still debatable, and their role in governing CH_4 conversion remains unclear. Herein, this study answers these questions using bimetallic catalysts by novel electro-shock strategy with controllable GBs for the oxidization of $Cu^{\delta+}$ species by modulating Ag loading. The Ag enrichment at the GBs facilitates the bonding of oxygen with the uncoordinated Cu atoms, resulting in GB oxidation effect. The obtained CH_4 selectivity is twice that of GBs or nanoalloy effect. The enhanced performance is attributed to the stable $Cu^{\delta+}$ species and unique electron transfer mechanism from GB oxidation structure. *Operando* attenuated-total-reflection Fourier-transform-infrared-spectroscopy unveils the reaction pathway of CO_2-to-CH_4 and the sluggish reversible quenching processes of intermediates. Theoretical calculations indicate that the weak *CO adsorption on GB oxidation structure facilitates *CO hydrogenation, promoting CO_2-to-CH_4 conversion.

1. Introduction

Electrochemical CO_2 reduction (ECR) into value-added chemicals and fuels using renewable resources helps tackle the challenges of energy crisis and global warming, but this strategy highly depends on the design and fabrication of electrocatalysts with great activity and selectivity to minimize the energy consumption [1–4]. Among the state-of-the-art ECR catalysts, copper is the only metal capable of reducing CO_2 into hydrocarbons and alcohols [5]. Therefore, numerous approaches, including alloying [6,7], oxide-derived copper (OD-Cu) [8,9], grain boundaries (GBs) [10,11], morphology modification [12,13], and

interface and strain engineering [14,15], have been developed to increase the capability of the Cu-based catalysts. The main technique of these approaches is to create specific ensembles with controllable selectivity towards the targeted products (e.g. ethylene and methane). Nevertheless, the structure-performance relationship between electrocatalysts and the activity and selectivity of ECR remain unclear, hindering the development of Cu-based catalysts [4].

Among the preceding strategies for catalyst design, GBs are widely used to tune the activity and selectivity of ECR [10,16]. The GBs, as one of structural defects, can create substantial structural perturbations in their vicinity, strained regions, and high-energy surfaces for catalysis

---

[17]. Thus, one of the essential tasks in catalyst design is to enhance the density of GBs to manipulate each mechanistic step of the ECR reactions. The GBs generated from OD-Cu have attracted significant attention among the previous preparation protocols [8,9]. During *in-situ* reduction of oxide/hydroxide crystals into nanosized irregular Cu grains, this method can be used to produce rich GBs accounting for the enhanced selectivity of C_{2+} products, such as ethylene and ethanol [8]. Moreover, previous studies indicate that the density of the GBs on the surface of OD-Cu directly correlates with the binding energy of the key intermediate (e.g.,*CO), greatly expediting the reactions and promoting C–C coupling [10,18].

According to the Pourbaix diagram of Cu metal, oxidized Cu precursors should be completely reduced to metallic Cu(0) when negative potentials are applied [19]. However, the presence of $Cu^{\delta+}$ species and copper oxide has been reported under ECR conditions [20,21]. These earlier experimental results suggest that these species are persistent during ECR, acting as active sites for high C_{2+} selectivity [22]. Nonetheless, other experimental studies show that only metallic Cu exists at the reduction potential in ECR [23,24]. These conflicting statements in the literature indicate the difficulty to accurately identify the active sites of OD-Cu in ECR.

To date, although the grain boundaries was considered to tune the electrocatalytic activity and selectivity of OD-Cu [25], the GB oxidation effect remains unclear in the OD-Cu system. Highly active GBs at the small Cu grains are usually unstable and liable to oxidation, although high-density GBs on the catalyst surface are desired [26,27]. For example, the uncoordinated Cu atoms on the GBs in Cu-Ag thin-film are susceptible to spontaneous oxidation in the ambient air, but the oxidized GBs degrade the Faradaic efficiency (FE) of CO and CH_4 in neutral electrolyte [28]. However, quantum mechanics indicates that the borders of the oxidized and metallic Cu surface regions in the oxidized matrix significantly enhances the ECR activity [29]. Although OD-Cu catalyst system are generally believed to promote C–C coupling toward C_2 products [20–22], this mechanism does not apply to the reaction system of C_1 products like CO and CH_4, especially in the Cu-based bimetallic alloy catalysts. Incorporating oxygen into the GBs in bimetallic CuAg alloys further complicates the alloy system because of the compatibility of Cu_2O, CuO and Ag_2O [30]. Thus, the conflicting conclusion reported in the literature indicate the challenges to understanding the role of GB effect and oxidation states on the activity and selectivity of ECR to CH_4 in pH-neutral electrolyte.

This work presents an electro-shock (ES) reduction strategy for the synthesis of bimetallic nanoparticles. By ES reduction, three distinct forms of CuAg nanoparticles with unique structural features (such as GBs, or GB oxidation, or nanoalloy) exhibit different ECR activities, highlighting the superiority of GB oxidation structure. Notably, the similar ECR performance of ES-Cu and ES-50 %CuAg samples indicates that the nanoalloy effect does not dominate the reaction pathway of ECR to CH_4, but the GBs do. The incorporation of oxidation effect into GBs in the ES-1 %CuAg significantly improves the FE of CH_4, which is twice higher than that of ES-Cu or ES-50 %CuAg. We have unraveled the mechanism underlying the GB oxidation effect during ECR using *operando* X-ray absorption spectroscopy (XAS) and ATR FT-IR spectra. Our findings highlight the role of steady-state $Cu^{\delta+}$ species play as active sites in ECR, and the unique electron transfer mechanism facilitated by Cu–O bridge at GBs rather than the Cu-Ag bond. DFT calculations further validate the significance of weak *CO adsorption in promoting the conversion of ECR to CH_4. These deep understanding of GB oxidation effect helps clarify the conflicting conclusions in the literature, and sheds light on the design and synthesis of GB oxidation structure for effective ECR.

2. Experimental and computational methods

2.1. Materials

Copper(II) chloride dihydrate ($CuCl_2 \cdot 2H_2O$), silver nitrate ($AgNO_3$), 60–80 nm Cu nanoparticles and potassium bicarbonate ($KHCO_3$) were purchased from Sigma-Aldrich (Canada). Nitric acid (HNO_3), ethanol, ultrapure water (18 MΩ cm), and *iso*-propanol were obtained from the chemical store on the University of Waterloo campus. Carbon cloth without microporous layer (MPL) was purchased from fuel cell store, USA. Argon and CO_2 gas were purchased from Linde Gas, Canada.

2.2. Synthesis of CuAg alloy nanoparticles

An electro-shock method was developed to synthesize CuAg nanoparticles following these steps. First, 0.5x1 cm^2 carbon cloth was activated in a 100 mL of 2 M nitric acid (HNO_3) solution with constant stirring at 120 ℃ for 2 h. After activation, the resulting carbon cloth was successively washed three times with water and ethanol until reaching constant pH, and the air-dried for later use. Second, for the preparation of the 10 mM metal precursor solution, $CuCl_2$ and $AgNO_3$ were dissolved into ethanol and mixed solvent (water/ethanol = 1:3), respectively. Then the precursor solutions with targeted loading concentrations (Cu: Ag = 99:1, 100uL total volume) were sequentially sprayed onto the activated carbon cloth. The samples were left to dry at room temperature before electric shock using a Metrohm autolab (PGSTAT204) with the 10A booster as an external power source, with a current of up to 10A. A 10 A current for 0.1 s under argon protective gas was selected as the reaction condition for synthesizing the ES-1 %CuAg electrocatalysts. The ES-Cu, ES-Ag, and ES-50 %CuAg were prepared using same method, with only the volume ration of Cu and Ag metal precursor solution being varied, such as ES-Cu for 100 %Cu, ES-Ag for 100 %Ag, ES-50 %CuAg for Cu:Ag = 1:1.

For control experiment, WC-1 %CuAg nanoparticles were prepared by a standard wet chemical method. First, 10 mg of commercial Cu nanoparticles were dispersed in 5 mL of ethylene glycol. Then, 0.5 mg of $AgNO_3$ was added to the above solution, which was then sonicated for 1 h. The resultant WC-1 %CuAg nanoparticles were washed three times by water and ethanol, respectively, followed by drying for 12 h under vacuum at 60 ℃.

2.3. Ex-situ material characterization

Scanning electron microscopy (SEM, Hitachi S4800, Japan) images were conducted under a working accelerating voltage of 10 kV. Glancing-incidence X-ray diffraction (GIXRD) spectra were performed on a MRD diffractometer (PANalytical X'Pert Pro, Netherlands) with Cu Kα radiation (1.54 Å) at an incidence angle of 0.3°. X-ray photoelectron spectroscopy (XPS) measurements were carried out (Thermo-VG Scientific ESCALab 250, USA) using microprobes with a monochromatic Al Kα X-ray source (1486.6 eV). High-angle annular dark-field scanning TEM (HAADF-STEM) and EDS images (FEI Titan 80-300 HB TEM/STEM, USA) were taken with an aberration corrector operating at 60 kV accelerating voltage. High resolution TEM images (Zeiss Libra 200MC, German) were collected under an acceleration voltage of 200 kV. Inductively coupled plasma mass spectrometry (ICP-MS) analysis was performed on an Agilent 8800 triple quadrupole, using He as a collision cell gas, Ge and In and In as internal standards to calibrate for instrument drift and ICP elemental standards to verify the accuracy of the instrument. Proton nuclear magnetic resonance (H-NMR) was run on Bruker Avance III 500 MHz, USA. The reduced products were evaluated on a gas chromatograph (Agilent 6890, USA) with a Carbonxen® 1000 column and a CarbonPLOT column for flame ionization detector (FID) and thermal conductivity detector (TCD), respectively.

2.4. Electrochemical measurements

All electrochemical tests were conducted on an electrochemical workstation (Gamry Reference 3000, USA) with IR compensation at room temperature. The customized H-type cell composed of two compartments separated by the Nafion 211 membrane. An Ag/AgCl reference electrode, Pt counter electrode, and $0.5 \times 1 \text{ cm}^2$ carbon cloth served as reference electrode, counter electrode and working electrode, respectively. The 0.1 M $KHCO_3$ electrolyte was saturated by bubbling CO_2 for 30 min before test. The ECR catalytic activities were evaluated under an applied cathodic potential for 1000 s with 10 sccm of flowing pure CO_2 gas. The gas products were characterized by the Agilent 6890. The liquid products were characterized with a Bruker 500 MHz Nuclear Magnetic Resonance (NMR) using an internal reference prepared with D_2O and DMSO.

All potentials in this work were measured against the Ag/AgCl reference electrode and converted into reversible hydrogen potential (RHE) using the equation below:

$$E\,(\text{vs. RHE}) = E\,(\text{vs. Ag/AgCl}) + 0.059 \times pH + 0.197$$

All the potentials are relative to the RHE unless stated otherwise.

2.5. Operando XAS measurements

The *operando* XAS measurements were conducted at 06ID-1 Hard x-ray MicroAnalysis (HXMA) beamline of the Canadian Light Source (CLS) operated at 2.9 GeV with a constant current of 250 mA. The measurements at the copper K-edge and Ag K-edge were performed in fluorescence mode using a Lytle detector. The ECR was carried out in CO_2-saturated 0.1 M $KHCO_3$ solution with 10 sccm of flowing pure CO_2 gas in a home-made cell. *Operando* XAS measurements was recorded at applied cathodic potential from 0 V to −1.1 V vs RHE. The XAS data were fitting using the software package Athena. During the fitting process, the k^3 weighting, k-range of $3 \sim 12.5$ Å^{-1} and R range of $1 \sim 3$ Å were used for the fitting of Cu-foil; The k^3 weighting, k-range of $3 \sim 12$ Å^{-1} and R range of $1 \sim 3$ Å were used for the fitting of as-prepared samples.

2.6. Operando time-dependent EPR measurement

Time-dependent continuous-wave (CW) EPR measurements at X-band frequencies (9.4 GHz) were performed using Bruker EMX Micro EPR spectrometer. DMPO was used as a spin trap. Electrochemistry procedures were performed with ES-1 %CuAg in the CO_2-saturated 0.1 M $KHCO_3$ electrolyte containing 10 mM of DMPO. During ECR reaction, 10 uL of samples were taken from the electrochemical cell and transferred into 1 mm ID, 2 mm OD EPR tube (712-SQ-100M Wilmad Lab-Glass). For the EPR measurements these tubes were placed into 3 mm ID 4 mm OD EPR tubes (707-SQ-250M Wilmad LabGlass). For all the measurements microwave power was set to 1.262 mW (22 dB microwave power attenuation) and modulation amplitude was 2 G at 100 kHz modulation frequency. Simulations of the EPR spectra were performed with EasySpin software [31].

2.7. Operando ATR FT-IR measurements

The measurements were conducted at 02B1-1 Far-IR beamline of the Canadian Light Source (CLS). *Operando* ATR FT-IR were run using a Bruker IFS 125 HR spectrometer with a 9.4 m OPD with a custom-built Veemax III variable angle reflectance system (Pike instruments), and all spectra were given by the absorbance [-log(R/R$_0$)]. The catalyst ink was dropped via pipette onto an ITO-coated SI Microgrooved Wafer Element with a 55° Face angle and then left to dry in air before test. A platinum wire and an Ag/AgCl electrode were used as counter and reference electrodes, respectively. The 0.1 M $KHCO_3$ electrolyte was constantly purged with CO_2 during the measurement. The applied cathodic potentials were changed from −0.1 V to −1.7 V, and the infrared spectra

were collected with a time resolution of 2 min per spectrum.

2.8. DFT Computational Details

All spin-polarized DFT calculations were performed within the Vienna Ab initio Simulation Package (VASP) using the projector augmented wave method [32]. The generalized gradient approximation (GGA) of Perdew-Burke-Ernzerhof (PBE) was used to describe the exchange and correlation effects [33]. A kinetic energy cutoff of 500 eV was used to set the plane-wave basis set. A Gaussian smearing of the width of 0.05 eV was used during calculations. Geometrical optimizations stopped when the energy convergence was less than 10^{-6} eV and the forces on each atom were less than 0.005 eV/Å. The $3 \times 1 \times 1$ and $9 \times 3 \times 1$ Monkhorst − Pack k-point meshes were used for geometrical optimizations and electronic properties calculations, respectively. The van der Waals interactions were corrected by the Grimme's DFT-D3 method [34]. A vacuum space of 15 Å was added along the *z* axis to avoid the interlayer interactions. The free energy (ΔG) was determined by $\Delta G = \Delta E + \Delta ZPE - T\Delta S$ [35], where ΔE is the reaction energy, ΔZPE is the change of zero-point energy, *T* is the temperature (298.15 K), and ΔS is the change of entropy.

3. Results

3.1. Synthesis and ex-situ characterization of electrocatalyst

The metal-precursor solution is sprayed sequentially onto an activated carbon cloth, which is subject to the Joule heating created by 0.1 s of electric shock. The thermal shock breaks down the metal salts [$CuCl_2$ and $AgNO_3$] into Cu and Ag atoms in only 0.1 s. The rapid thermal shock prevents Cu and Ag atoms from diffusing to form an equilibrium phase. However, the surface defects and oxygen-containing functional groups in the activated carbon cloth create kinetic anchoring sites. As a result, high-temperature mixing entropy drives the Cu and Ag atoms to mix, forming non-equilibrium bimetallic nanoparticles (Fig. 1a).

The scanning electron microscope (SEM) images (Figs. 1b, c and S1–S3) reveal the resultant *in situ* growth of many spherical CuAg nanoparticles on the activated carbon cloth. In a typical synthesis process, lowering the concentration of the Cu metal precursor solution greatly reduces the surface distribution and sizes of the spherical Cu nanoparticles on the carbon cloth because of insufficient Cu metal sources (Fig. S1a–d). However, the size of ES-Ag nanoparticles (Fig. S2a and b) are significantly larger than the ES-Cu nanoparticles (Fig. S2c and d). The same reaction conditions with different metallic elements indicate that Ag atoms tend to aggregate more. As shown in Fig. S3a and b, the nanoparticles formed at 0.05 s of electric shock are relatively small with extremely low surface coverage, indicating that 0.05 s of electric shock is insufficient for adequate migration and nucleation of metal atoms. However, extending the electro-shock time (> 0.1 s) promotes the nucleation and overgrowth of nanoparticles, resulting in a decrease in surface distribution (Fig. S3c–f). Based on the experimental results, 0.1 s of electric shock is the optimal for synthesizing bimetallic CuAg nanoparticles. After the introduction of Ag into Cu matrix (Figs. 1b, c and S4a–f), the ES-1 %CuAg (Fig. S4c and d) and ES-50 % CuAg (Fig. S4e and f) exhibit much higher surface dispersibility than that of ES-Cu (Fig. S4a and b), indicating that adding silver significantly enhances the nucleation rate of nanoparticles, even at low concentrations, while excessive Ag loading would cause the CuAg nanoparticles to grow larger (Fig. S4c and d vs Fig. S4e and f).

The composition and structure features of the prepared samples were further studies using grazing incidence X-ray diffraction (GIXRD). No Ag reflection is observed in GIXRD pattern because of the low Ag loading and sample content on the carbon cloth, and the strong background signal (25.5° and 54°) from the carbon cloth support results in a large baseline that affects the quality of the Cu signals (Fig. 1d). Compared to the GIXRD patterns of Cu nanoparticles and WC-1 %CuAg nanoparticles
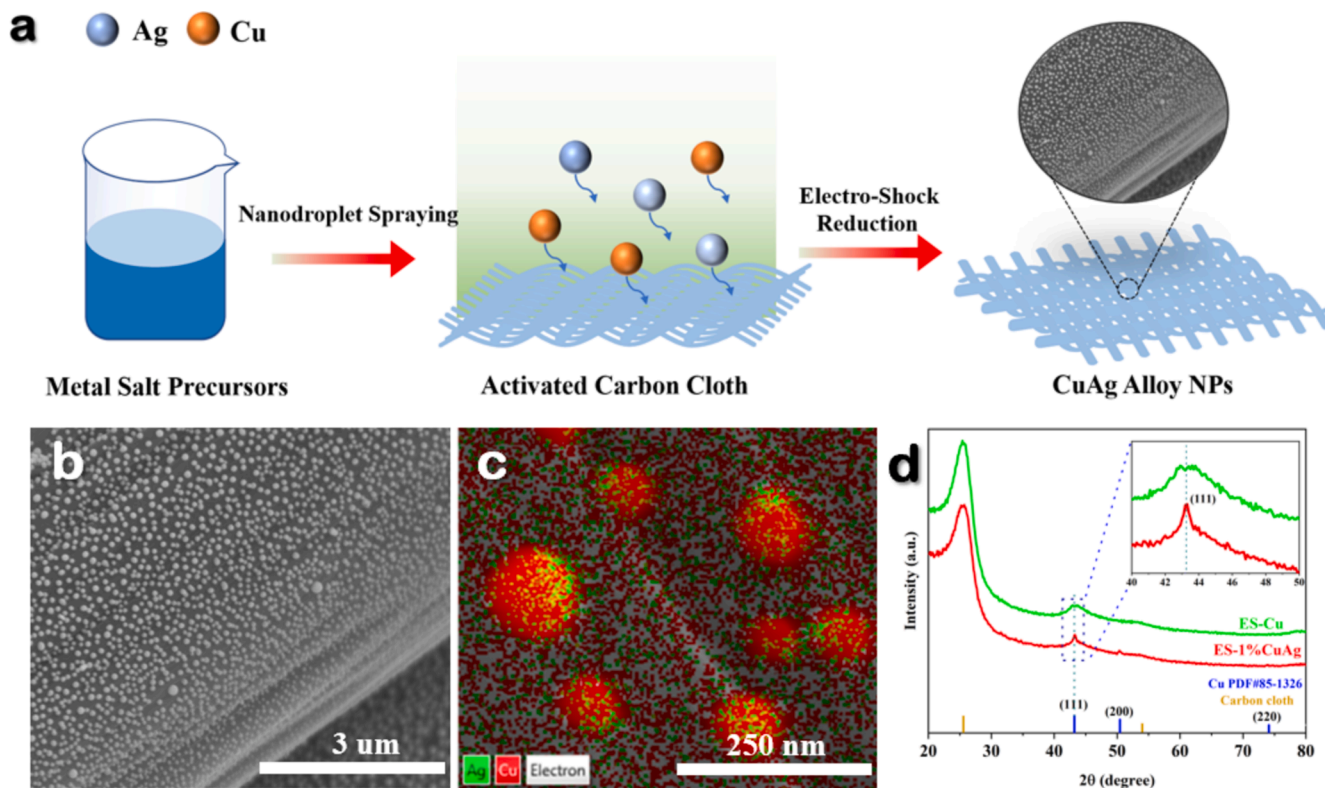
Fig. 1. Synthesis and structural characterization of electrocatalysts. (a) Scheme of the synthesis processes of CuAg catalysts by electro-shock method; (b) SEM image and (c) corresponding EDS element mapping image of ES-1%CuAg sample; (d) GIXRD spectra of ES-Cu and ES-1%CuAg.

prepared by wet chemistry (WC) method (**Methods**, **Fig. S5**), the absence of Cu_2O peaks at 36.3° and 61.2° (Fig. 1d) indicates that solid-solution structure and entropy effect causes the ES-Cu and ES-1 %CuAg to exhibit a different atomic arrangement from that of the WC-1 %CuAg. The ICP-MS results show that the Ag content in ES-1 %CuAg and ES-50 %CuAg is 1.7 wt% and 47.5 wt% (**Table S1**), respectively. The aberration corrected-high-angle annular dark-field scanning transmission electron microscopy (AC-HAADF-STEM) (Fig. 2a and b) and high-resolution transmission electron microscopy (HRTEM) (**Fig. S6a–c**) images reveal the existence of GBs in all samples. Notably, the ES-Cu also exhibits the GBs structure (**Fig. S6a**), indicating that solid-solution structure induced by the electro-shock method is a non-equilibrium phase, and the metal atoms is randomly distributed. ES-1 %CuAg (Fig. 2a) and ES-50 %CuAg (Fig. 2b) show a face-centered cubic (fcc) crystalline structure with $d_{(111)}$ spacing of 0.22 and 0.23 nm between the spacing values of Cu and Ag metals, respectively [36]. Energy-dispersive x-ray spectroscopy (EDS) elemental mapping images reveal the rich accumulation of Ag and oxygen atoms on the GBs, as well as bulk distribution of oxygen atoms across grains, in the ES-1 %CuAg (Figs. 2c and **S7a**). This indicates that the Ag and oxygen enrichment on the GBs allows for the incorporation of oxygen into the defect structure, subsequently triggering the oxidation of unsaturated Cu sites. In contrast, the homogeneous distribution of Cu and Ag atoms and the absence of oxygen atoms in the ES-50 %CuAg suggest that the nanoalloy effect prevents Cu sites on GBs from oxidation (Figs. 2d and **S7b**). As a result, the non-uniform distribution of Ag atoms in Cu matrix for the ES-1 %CuAg serves as a prerequisite for the oxidation of Cu sites on the GBs.

The surface compositions and chemical states of the as-prepared catalysts were further characterized using X-ray photoelectron spectroscopy (XPS) (Figs. 3a and **S8a–f**). The Cu $2p_{3/2}$ spectra of all samples can be deconvoluted into two peaks, corresponding to Cu^+/Cu^0 and Cu^{2+} peaks, respectively. The intensity ratio of Cu^{2+} to Cu^+/Cu^0 peaks for ES-1 %CuAg is 11.45, which is higher than those of ES-Cu (2.08) and ES-50 %CuAg (0.74) (Fig. 3a). This indicates that under the GB

oxidation effect, the surface copper sites undergo further oxidation when exposed to air during *ex-situ* characterization. Moreover, the peak position of Cu^+/Cu^0 shifts towards a higher binding energy from 932.4 eV (ES-Cu) to 932.6 eV (ES-1 %CuAg) and 932.8 eV (ES-50 %CuAg) (Fig. 3a), suggesting that the interaction between the Cu and Ag sites affects the surface electronic structure of the Cu atoms [37]. In contrast, for WC-1 %CuAg, the absence of Cu^+/Cu^0 signal and the unshifted binding energy of Cu^{2+} indicate a stronger electron attraction effect of Ag in equilibrium phase (**Fig. S8a**). Regarding O 1 s XPS spectra, lattice oxygen observed in Cu nanoparticles and WC-1 %CuAg is not present in ES-Cu, ES-1 %CuAg and ES-50 %CuAg (**Fig. S8b-c**). Notably, the Cu–O bond of ES-1 %CuAg shifts to a position with higher binding energy (532.4 eV) compared to ES-Cu (531.7 eV) and ES-50 %CuAg (531.8 eV) (**Fig. S8c**). This indicates that the GBs in ES-1 %CuAg readily bind with oxygen, inducing stronger oxidation effect. Due to the inert atmosphere during synthesis, the source of oxygen can be attributed to the oxygen-containing groups on the activated carbon cloth (**Fig. S8c and d**). Therefore, the oxygen-containing groups not only provide anchoring sites, but also are involved in the nucleation and growth of nanoparticles by bonding to unsaturated Cu sites. Compared to the binding energy of Ag 3d at 368.4 eV for ES-1 %CuAg and ES-50 %CuAg (**Fig. S8e**), the binding energy of Ag 3d for WC-1 %CuAg shifts to 369.5 eV (**Fig. S8f**), indicating that the non-equilibrium phase exhibits completely different electronic structure and charge distribution between Cu and Ag from equilibrium phase [37].

Because the XPS is insufficient to accurately determine the oxidation state and local coordination environment of the Cu and Ag species under high dispersion and low loading, synchrotron-based X-ray absorption Near-Edge Structure (XANES) spectra and Extended X-ray Absorption Fine Structure (EXAFS) spectra were performed to further investigate the GB oxidation effect. Compared to the Cu foil and Cu_2O reference, the XANES spectra of ES-Cu and ES-50 %CuAg exhibit characteristics of metallic Cu, while the Cu oxidation state in ES-1 %CuAg is close to the Cu(I) state ($Cu^{\delta+}$, $0 < \delta < 1$) (Fig. 3b). The Ag loading significantly
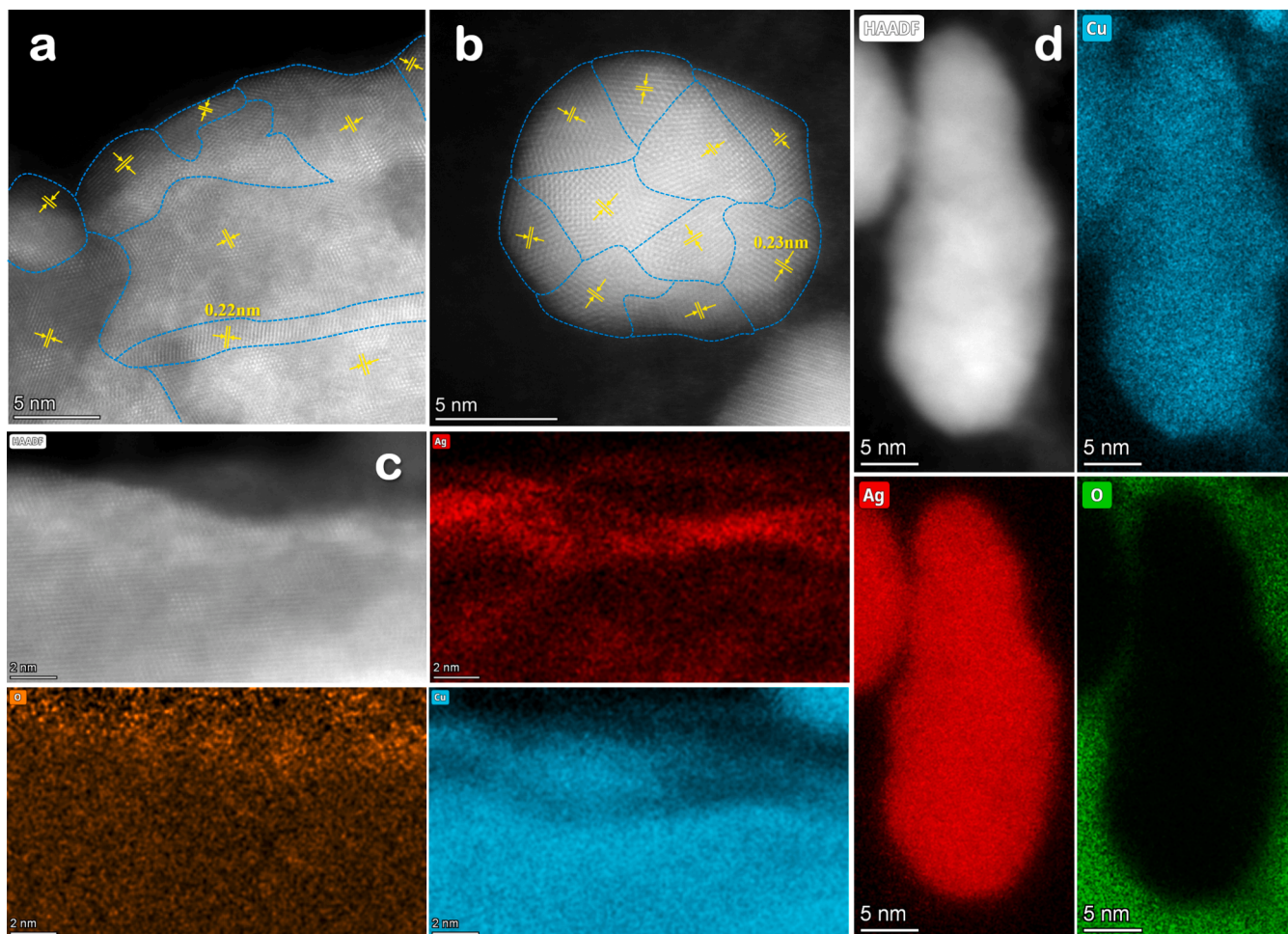
Fig. 2. AC-HAADF-STEM and EDX images of electrocatalysts. (a,b) AC-HAADF-STEM images of (a) ES-1%CuAg and (b) ES-50%CuAg, respectively. (c,d) STEM-EDX element mapping image of (c) ES-1%CuAg and (d) ES-50%CuAg, respectively.

changes the valence state of Cu sites. Conversely, the Ag K-edge XANES spectrum of ES-1 %CuAg is also completely different from that of Ag foil and ES-50 %CuAg (Fig. 3c), indicating strong interaction between Ag and Cu. The coordination environment of Cu sites in all samples was further investigated through the structural parameters obtained from quantitative fitting of the EXAFS spectra (Figs. 3d, **S9** and **Table S2**). The absence of Cu–O bond in ES-Cu and ES-50 %CuAg further differentiate the presence of Cu–O bond induced via GBs oxidation effect in ES-1 %CuAg. Compared to Cu foil, the similar Cu-Cu bond distance (R_{Cu-Cu} = ~2.53 Å) but significantly different Cu-Cu coordination number (N_{Cu-Cu} = ~3.8) in ES-Cu indicates that Cu sites in ES-Cu are in a lower coordination state (**Table S2**). Since the catalyst prepared via electro-shock synthesis is a non-equilibrium phase with randomly mixed atoms, the catalyst is rich in GBs structures, leading to low-coordinated Cu sites.

3.2. Operando multimodal characterization of electrocatalysts for ECR in neutral media

Operando XAS was performed to reveal the structure evolution and charge transfer between Cu and Ag atoms during ECR. The *operando* Cu K-edge XANES spectra of ES-1 %CuAg in CO_2-saturated 0.1 M $KHCO_3$ solution show a similar shape and position under open circuit potential (OCP) and cathodic potentials of −0.6 V_{RHE}, −0.9 V_{RHE} and −1.1 V_{RHE} (Fig. 4a). Although the oxidation state of $Cu^{\delta+}$ species presents a downward trend (see inset in Fig. 4a), the $Cu^{\delta+}$ species are incompletely reduced to metallic Cu, even at high cathodic potentials. This indicates

that the GBs structure introduced by electro-shock synthesis contributes to the structural stability and resistance to the electrochemical reduction under reduction potentials in ECR. Therefore, ES-Cu and ES-50 %CuAg show the similar stability for $Cu^{\delta+}$ species during ECR (**Figs. S10** and **S11a**). Additionally, despite the dominant Cu-Cu bond in ES-Cu and ES-50 %CuAg before reaction, the metallic Cu undergoes rapid oxidation to $Cu^{\delta+}$ species under ECR reaction (**Figs. S10** and **S11a**). This indicates that the *in-situ* generated strongly oxidative species (e.g. OH radicals) lead to the oxidation of copper sites in the CO_2-saturated 0.1 M $KHCO_3$ electrolyte [38–40].

To extent the study further, *operando* Ag K-edge XANES spectra were collected (**Figs. 4b** and **S11b**). The results obtained from ES-50 %CuAg show electron transfer from electron-rich Ag to electron-deficient Cu during the ECR (**Fig. S11a and b**). However, regarding ES-1 %CuAg, it is noteworthy that the Ag K-edge absorption spectra (Fig. 4b) still indicate a reducing effect similar to that observed in Cu K-edge spectra (Fig. 4a), which indicates that the electron transfer is not from Ag to Cu in the ES-1 %CuAg. Such a different behavior between ES-50 %CuAg and ES-1 %CuAg can be attributed to the GB oxidation effect in ES-1 %CuAg. In the ES-1 %CuAg, oxygen interacts with the surface electrons of the Cu and Ag atoms, driving electron transfer from electron-rich O to electron-deficient Cu and Ag. This electron transfer may alter the electronic structure and chemical properties of the Cu sites, enhancing ECR activity. Moreover, this mechanism behind electron transfer from O to Cu/Ag atoms in ES-1 %CuAg significantly differs from that observed in ES-50 %CuAg and those previously reported in the literature [37,41].

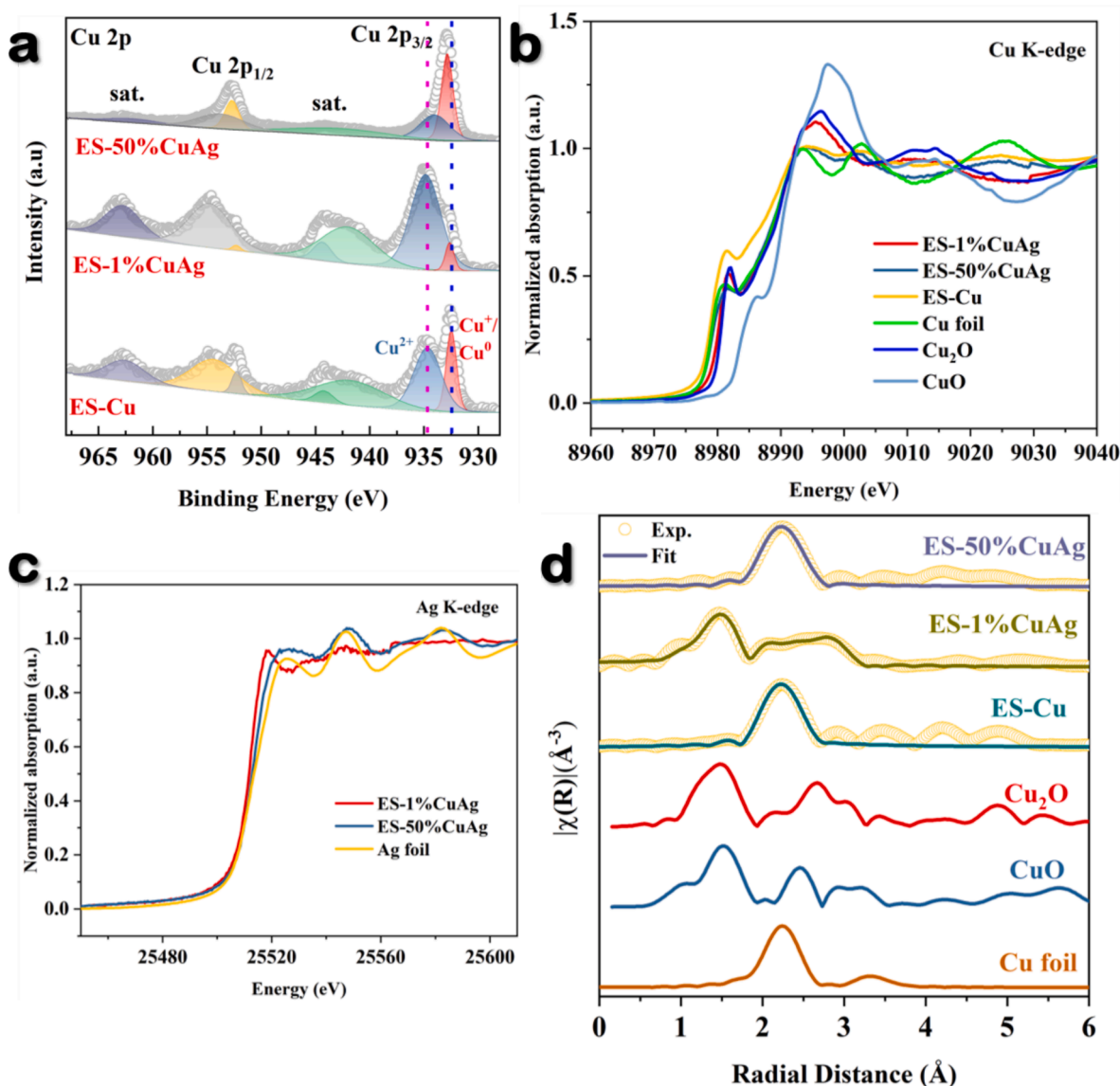To confirm the impact of strongly oxidative species in the CO_2-

Fig. 3. *Ex situ* **X ray spectroscopic analysis of electrocatalysts.** (a) Cu 2p XPS spectra of ES-Cu, ES-1 %CuAg and ES-50 %CuAg catalysts; (b) Cu K-edge XANES spectra of ES-Cu, ES-1 %CuAg and ES-50 %CuAg samples and corresponding references (Cu foil, Cu_2O, and CuO); (c) Ag K-edge XANES spectra of ES-1 %CuAg and ES-50 %CuAg and corresponding references (Ag foil); (d) Cu K-edge EXAFS experimental and fitting spectrum and of ES-Cu, ES-1 %CuAg and ES-50 %CuAg catalysts and corresponding references (Cu foil, Cu_2O, CuO).

saturated 0.1 M $KHCO_3$ electrolyte on the rapid oxidation of active Cu sites during ECR, *operando* time-dependent electron paramagnetic resonance (EPR) was conducted (Fig. 4c). 5,5-dimethyl-1-pyrroline N-oxide (DMPO) is used to prolong the lifetime of the radicals to the minute range. When the electrolyte contains 10 mM DMPO, an electrode potential of -0.8 V_{RHE} applied on ES-1 %CuAg leads to hydrogen evolution reaction (HER) and subsequent trapping of hydrogen radicals (H) in the form of a DMPO-H adduct (hyperfine splitting constants, $A_N = 16.4$ mT, $A_H = 2.26$ mT) [38]. Upon switching to OCP, OH radicals appear as a DMPO-OH adduct ($A_N = 1.50$ mT, $A_H = 1.48$ mT) and become dominant after 1.5 h, persisting throughout the OCP process [38]. This finding provides further evidence that, during the ECR reaction, the OH radicals generated from electrolyte excitation act as potent *in-situ* oxidizing species, leading to the rapid oxidation of active Cu sites.

To detect the reaction intermediates during the ECR process, *operando* attenuated total reflection Fourier transform infrared spectroscopy (ATR FT-IR) measurement was performed for ES-1 %CuAg. The adsorption bands at 796 cm^{-1}, 1267 cm^{-1}, and 1318 cm^{-1} are assigned to $\delta(OCO)$, OH deformation, and C–O stretch, respectively (Fig. 4d).

They are generally considered as the important intermediates during ECR to CO or CH_4 [42,43]. The characteristic peak at 2143 cm^{-1} belongs to the adsorbed *CO, which would undergo further proton-coupled electron transfer (PCET) process [44]. This evolution is further confirmed by the *CH_3O group adsorption bands at 1020 cm^{-1} and 1140 cm^{-1} and the peak of *CHO group at 1060 cm^{-1} (Fig. 4d); both of them are critical intermediates for ECR to CH_4 [45,46]. Therefore, based on the *operando* ATR FT-IR spectra analysis (Fig. 4d), the most likely reaction pathway for ECR to CH_4 are proposed as followed. Firstly, dissolved CO_2 in the liquid electrolyte is absorbed, activated on the catalytic sites, and transformed into *COOH by PCET process. Then, the hydrogen bonds-stabilized *COOH intermediate releases a water molecule to form *CO intermediate via PCET. Subsequently, *CO intermediate is still absorbed on the active sites by a hydrogen bond and undergoes a series of PCET processes to produce *CHO and *CH_3O intermediates, finally leading to selective production of CH_4.

In addition, the real-time ATR FT-IR spectra were used to monitor the intermediate adsorption processes at electrode–electrolyte interface. The *operando* real-time ATR FT-IR spectra were collected every two
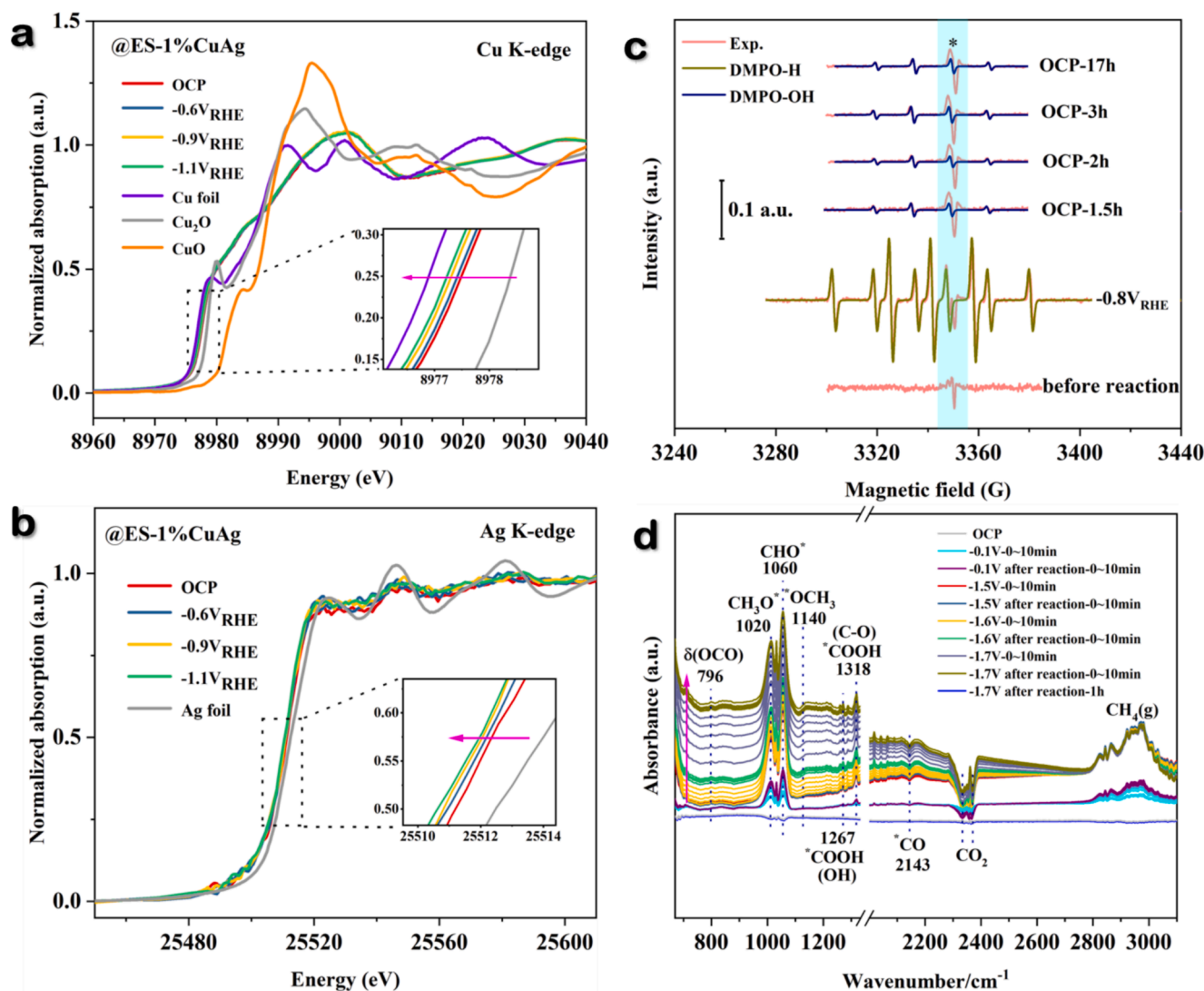
Fig. 4. *Operando* **multimodal characterizations of electrocatalysts during ECR in neutral media.** (a) *operando* Cu K-edge XANES spectra and (b) *operando* Ag K-edge XANES spectra of ES-1 %CuAg under OCP and cathodic potentials from $-0.6V_{RHE}$, $-0.9V_{RHE}$ to $-1.1V_{RHE}$; (c) *operando* time-dependent normalized EPR spectra of 0.1 M KHCO$_3$ electrolyte at $-0.8V_{RHE}$, followed by switching to OCP for different periods on ES-1 %CuAg sample. Experimental spectra are depicted in red, while simulated spectra are depicted in blue and dark yellow for DMPO-OH and DMPO-H radicals, respectively. EPR signals marked by asterisk is from the sample tube. (d) *Operando* ATR FT-IR spectra collected from ES-1 %CuAg catalyst at different applied potentials (-0.1 V, -1.5 V, 1.6 V and -1.7 V).

minutes during the application of potentials, as well as after the potential was turned off, in a CO$_2$-staturated 0.1 M KHCO$_3$ (Figs. 4d and S12a–d). The intermediate adsorption bands during ECR to CH$_4$ could be clearly observed even when the applied cathodic potential is as low as -0.1 V, indicating that -0.1 V can trigger the ECR reaction (Fig. 4d). With the increasing potentials or prolonging reaction time, the solubility of CO$_2$ further increases in the electrolyte, enhancing the intensity of intermediate characteristic peaks (**Fig. S12a–d**). Furthermore, it is deemed reasonable that intermediates adsorption during ECR is reversible, and the signals for intermediates promptly disappear with potential withdrawal. However, once potentials were off, all peaks in our system did not disappear intermediately (Figs. 4d and S12a–d). Instead, *in-situ* generated intermediates remained on the catalyst surface or in the electrolyte for one hour after reaction at -1.7 V (Figs. 4d and S12d). Combined with the *operando* Cu K-edge and Ag K-edge XAS, these results indicate that *in-situ* generated ECR intermediates adsorbed on the surface of ES-1 %CuAg, and that active Cu$^{\delta+}$ species promote the chemical evolution of adsorbate during ECR. However, potential withdrawal stops the continuous evolution. The sluggish reversible process indicates that active sites in turn prolongs the temporary existence of

intermediates in the electrolyte by hydrogen bond. Eventually, the intermediates either disappear or evolve into the final products.

3.3. Performance of ECR in neutral media

The ECR performance of the as-synthesized catalysts were evaluated. Comparative analysis reveals that ES-1 %CuAg exhibits the highest current density among all the catalysts (**Fig. S13a**), and the current density of ES-1 %CuAg in CO$_2$-saturated 0.1 M KHCO$_3$ electrolyte is higher than that in Ar-saturated 0.1 M KHCO$_3$ electrolyte, indicating the catalytic activity of ECR (**Fig. S13b**). In more detail, the major products are H$_2$, CO, CH$_4$, and C$_2$H$_4$ for all samples with minor formate and ethanol (Figs. 5a–d and S14a, b). Similar volcano-shaped curves trends for CO, C$_2$H$_4$ and CH$_4$ FEs on a wide range of applied potentials can be observed for all the samples (Fig. 5a–c). In terms of CO production (Fig. 5a), adding Ag into Cu matrix could significantly improve CO FE by four times compared to ES-Cu, indicating that Ag does facilitate the CO production. Notably, there was no significant difference in ethylene selectivity across the entire potential window for all catalysts (Fig. 5b), indicating that our CuAg system does not favor C–C coupling towards
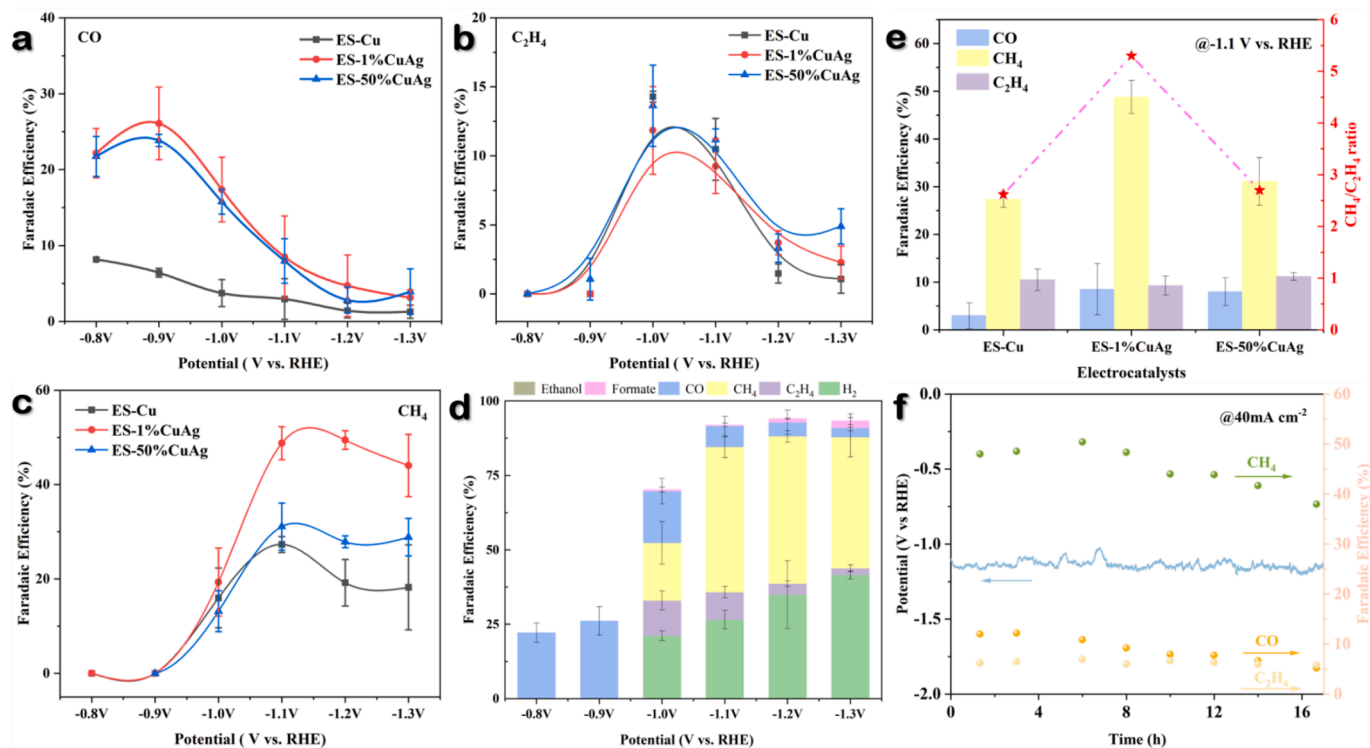
Fig. 5. Performance of ECR in neutral media. Comparison of Faradaic efficiency of (a) CO, (b) C_2H_4, and (c) CH_4 for ES-Cu, ES-1 %CuAg and ES-50 %CuAg samples. (d) Faradaic efficiency of reduced products on ES-1 %CuAg catalyst as a function of the electrode potential. (e) Comparison of Faradaic efficiency of CH_4, CO and C_2H_4 for ES-Cu, ES-1 %CuAg and ES-50 %CuAg under an applied potential of $-1.1V_{RHE}$. (f) The long-term stability test for ES-1 %CuAg catalyst at current density of 40 mA cm^{-2}.

ethylene formation. Therefore, ES-1 %CuAg shows the highest activity against CH_4 (~50 % FE at $-1.1V_{RHE}$) (Fig. 5c and d), which is nearly twice the CH_4 FE observed in ES-Cu and ES-50 %CuAg. This indicates that GB oxidation effect (ES-1 %CuAg) is stronger than GBs effect (ES-Cu) and nanoalloy effect (ES-50 %CuAg) on promoting the CH_4 reaction pathway in our system. Additionally, a comparative analysis was further conducted to evaluate the effect of non-equilibrium (ES-Cu, ES-1 %CuAg and ES-50 %CuAg) and equilibrium phases (commercial Cu and WC-1 % CuAg) on CH_4 and C_{2+} product selectivity (Figs. 5a–d **and S15a, b**). Compared to the non-equilibrium phase, the equilibrium phase system significantly promoted the selectivity of ethanol and formate (**Fig. S15a and b**). However, even with the introduction of Ag into the equilibrium phase system, it neither suppressed CH_4 formation nor enhanced the selectivity for ethylene and ethanol compared to commercial Cu NPs (**Figs. S15a vs S15b**). As reported in other literature, Ag-Cu surfaces rich in low-coordination sites and CuAg catalysts with unique electronic structures modulate the CO adsorption strength, selectively promoting CH_4 production [37,47]. Therefore, we can conclude that in the CuAg system with rich GBs structure, the unique GB oxidation structure is more favorable for CH_4 production, and the nanoalloy effect is not as effective in promoting the production of C_{2+} products in neutral electrolytes [1,41]. This indicates the GB oxidation structure facilitates the hydrogenation of *CO rather than C–C coupling via the tandem mechanism.

More specifically, the main reduced products of the as-synthesized non-equilibrium phase samples at $-1.1V_{RHE}$ were compared (Fig. 5e). Similar C_2H_4 and CH_4 FEs for ES-Cu and ES-50 %CuAg indicate that the nanoalloy effect does not effectively promote the selective production of C_2H_4 or CH_4 but rather the GBs. The CH_4/C_2H_4 ratio (i.e., 5.3) of ES-1 % CuAg almost doubles that of ES-Cu (i.e., 2.62) and ES-50 %CuAg (i.e., 2.7). Such a volcano-shaped dependence of CH_4/C_2H_4 ratio on the three samples highlights the superiority of GB oxidation structure in CH_4 conversion. Moreover, the CH_4/C_2H_4 ratio of the equilibrium phase

(~1.0 for commercial Cu and ~ 1.33 for WC-1 %CuAg) is much lower than that of the non-equilibrium phase, indicating that the equilibrium phase exhibits similar tendencies for CH_4 and C_2H_4, while the unique GB oxidation structure in the non-equilibrium phase helps break the linear scale relationship for C_1 and C_2 products, selectively promoting CH_4 conversion. Additionally, at -0.8 V_{RHE} and -0.9 V_{RHE}, the CO partial current density increases with increasing potentials, while after -1.0 V_{RHE}, the H_2 partial current density rises sharply, far exceeding the slowly increasing CO partial current density (**Fig. S16a–c**). In contrast to ES-Cu and ES-50 %CuAg, the CH_4 partial current density of ES-1 %CuAg is significantly higher than that of H_2, indicating that the GB oxidation effect can effectively suppress the HER. The slow increase in the CO partial current density, combined with the high partial current density of H_2 and CH_4, suggests that our CuAg system does not follow the one-pot tandem fashion proposed for Ag-Cu surfaces [47], where *CO produced by Ag migrates to Cu sites. Instead, CO_2 preferentially adsorbs at the low-coordination Cu sites at the GB oxidation structure, and the hydrogen-covered Cu surface drives the hydrogenation of *CO to form *CHO and *CH$_3$O intermediates, finally leading to CH_4 production.

The long-term stability test of ES-1 %CuAg in an H-cell was evaluated at a current density of 40 mA cm^{-2}. The catalyst was able to operate stably for 17 h, with the selectivity for methane gradually decreasing from the initial 48 % to 38 %, demonstrating a certain degree of stability (Fig. 5f). After the stability test, nanoparticles remained attached onto the surface of activated carbon cloth (**Fig. S17a–f**); however, a portion of the nanoparticles had clearly detached and dissolved into the electrolyte. Additionally, the catalyst structure and morphology underwent significant reconstruction (**Fig. S17a–f**), all of which contributed to the decline in activity.

3.4. Density functional theory (DFT) calculations

DFT calculations were performed to gain an atomic-level

understanding of the origin of high ECR activity of ES-1 %CuAg in comparison with ES-Cu and ES-50 %CuAg, where GBs of three catalysts were simulated based on the $\Sigma5(210)$ tilt GB model (Fig. 6a and S18). The following mechanism was assumed for CH_4 production on three catalysts consistent with the ATR FT-IR analysis on reaction intermediates (Fig. 4d):
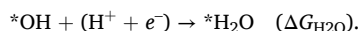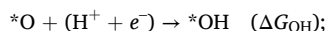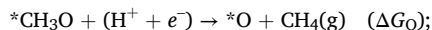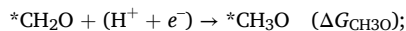
$$* + CO_2(g) + (H^+ + e^-) \rightarrow *COOH \quad (\Delta G_{COOH});$$

$$*COOH + (H^+ + e^-) \rightarrow *CO + H_2O \quad (\Delta G_{CO});$$

$$*CO + (H^+ + e^-) \rightarrow *CHO \quad (\Delta G_{CHO});$$

$$*CHO + (H^+ + e^-) \rightarrow *CH_2O \quad (\Delta G_{CH2O});$$

$$*CH_2O + (H^+ + e^-) \rightarrow *CH_3O \quad (\Delta G_{CH3O});$$

$$*CH_3O + (H^+ + e^-) \rightarrow *O + CH_4(g) \quad (\Delta G_O);$$

$$*O + (H^+ + e^-) \rightarrow *OH \quad (\Delta G_{OH});$$

$$*OH + (H^+ + e^-) \rightarrow *H_2O \quad (\Delta G_{H2O}).$$
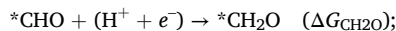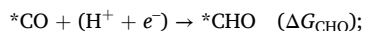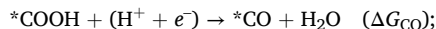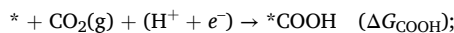
Fig. 6b displays the free energy diagram for all three examined model structures. The potential determining step (PDS) is *CO reduction for ES-Cu and ES-50 %CuAg with $\Delta G_{CHO} = 0.53$ eV and 0.54 eV, respectively, and is *CO_2 reduction to form *COOH for ES-1 %CuAg with $\Delta G_{COOH} = 0.45$ eV. We suggest that this shift in PDS is responsible for the better activity of ES-1 %CuAg. The adsorption free energy of *CO is a useful descriptor for understanding the differences in activity among the three structures, owing to the scaling relations between *CO and other ECR intermediates. We analyzed the Bader charges to gain a more detailed insight into the electronic structures of active Cu sites. Compared to the active Cu site in ES-Cu, the Bader charge for ES-50 %CuAg increases from $+ 0.02|e|$ to $+ 0.05|e|$, which aligns with the observed valence variation (Fig. 3b). For ES-1 %CuAg, weaker *CO adsorption can be attributed to the formation of Cu–O bonds induced by oxidation, resulting in a Bader charge of $+ 0.25|e|$ for the active Cu site. The weaker *CO adsorption on ES-1 %CuAg can be qualitatively illustrated by the fewest electron accumulation around the adsorbed *CO in the charge density difference plots (Fig. 6c) and quantitatively supported by the Bader charge analysis that 0.17, 0.12, and 0.21e transfer into *CO from ES-Cu, ES-1 %CuAg, and ES-50 %CuAg, respectively. Owing to the scaling relations, weaker *CO adsorption on ES-1 %CuAg results in weaker *CHO and *COOH adsorption leading to $\Delta G_{CHO} = 0.40$ eV and $\Delta G_{COOH} = 0.45$ eV (Fig. 6b). As a result, the PDS shifts from *CO $\rightarrow$ *CHO to $CO_2 \rightarrow$ *COOH. These results explain the role of GB oxidation in ES-1 %CuAg in enhancing ECR to CH_4. Moreover, the active $Cu^{\delta+}$ species in ES-1 %CuAg has the smallest valence variation during ECR (Fig. S19), suggesting the highly efficient valence regulation caused by nearby atoms in ES-1 %CuAg. Interestingly, for ES-1 %CuAg, the trend of valence variation of the O atom is nearly reverse to the active $Cu^{\delta+}$ species, further confirming that the electron transfer mechanism in ES-1 %CuAg is via the Cu–O bond, rather than Cu-Ag bond in ES-50 %CuAg during ECR (Fig. 6d).

4. Conclusions

In conclusion, a novel electro-shock method was developed for precise control of catalysts with GBs and GB oxidation structures. A 1 % Ag loading in Cu matrix leads to the Ag enrichment on the GBs, triggering the oxidation of Cu sites (i.e., GB oxidation effect). Performance
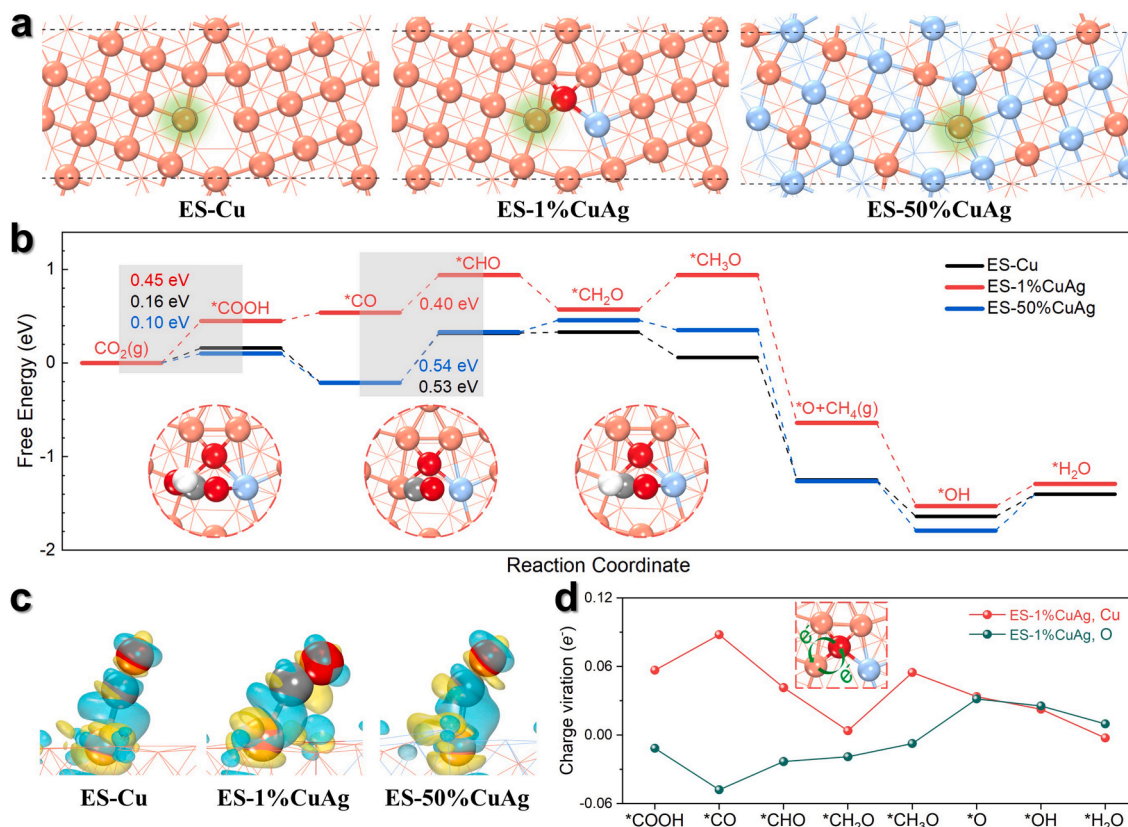

Fig. 6. Density functional theory calculations. (a) Top views of DFT model structures, where active Cu sites are highlighted in green. (b) Free energy diagram of ECR on ES-Cu, ES-1 %CuAg, and ES-50 %CuAg at the applied potential of 0 V, including *COOH, *CO and *CHO on ES-1 %CuAg. (c) Charge density difference plots of *CO with an isovalue of 0.001 $e/Å^{-3}$ on ES-Cu, ES-1 %CuAg, and ES-50 %CuAg, where cyan and yellow regions denote electron accumulation and depletion, respectively. (d) Bader charge variations of active Cu site and O atom in ES-1 %CuAg relative to the clean surface during ECR. Color code: Cu, coral; Ag, light blue; C, black; O, red; H, white.

comparisons among the nanoalloy, GBs, and GB oxidation effect highlight superiority of the GB oxidation structure. *Operando* XAS analysis reveals that, unlike nanoalloy or GBs effect, the performance improvement originates from the steady-state $Cu^{\delta+}$ species and a unique electron transfer mechanism induced by the GB oxidation effect. *Operando* ATR FT-IR spectra further uncover key intermediate *CHO and *CH$_3$O in CO_2-to-CH$_4$ conversion. DFT calculations the further confirm the weaker *CO adsorption on ES-1 %CuAg and highly efficient CH$_4$ conversion pathways. Overall, this work not only establishes the relationship between GB oxidation effect and CO_2-to-CH$_4$ conversion in bimetallic systems but also provides precise elucidation of active sites derived from CuAg system.

5. Code availability

All the DFT calculations were performed using commercial software VASP. All the input and output files of the calculations are available per request.

6. Additional information

Supplementary information is available for this paper. Correspondence and requests for materials should be addressed to C.V. S, Z. T., or Y. A. W.

Author contributions

Y.A.W. conceived and supervised the project. Z.T. co-supervised the project. C.V.S led the DFT calculations. L.W. carried out the catalyst's synthesis, characterization, and performance test. X.Y. and Y.X. conducted the DFT calculations. L.W., X.W, and Z.C. carried out the XAFS measurements and data fitting. D.A. helped with EPR measurements. C. D., Y.T., T.G., Y.Z., and J.P. assisted in the materials characterizations. N.C. and W.C. provided advice for the XAFS measurements. B. B. guided the ATR FT-IR test. K.M. and J.H.W provided advice on the STEM experiments. L.W., X.Y., C.V.S, Z. T., and Y. A. W. wrote the manuscript. All authors made comments and revised the manuscript.

CRediT authorship contribution statement

Lei Wang: Writing – original draft, Investigation, Formal analysis, Data curation. **Xue Yao:** Writing – original draft, Software, Formal analysis, Data curation. **Yi Xiao:** Investigation, Formal analysis. **Cheng Du:** Investigation, Formal analysis, Data curation. **Xiyang Wang:** Investigation, Formal analysis, Data curation. **Dmitry Akhmetzyanov:** Investigation, Formal analysis, Data curation. **Zuolong Chen:** Investigation, Formal analysis, Data curation. **Youchao Teng:** Investigation, Formal analysis, Data curation. **Tao Guo:** Data curation. **Yongzan Zhou:** Investigation, Data curation. **Joel P. Mills:** . **Ning Chen:** Writing – review & editing, Resources, Investigation. **Weifeng Chen:** Resources, Investigation. **Brant Billinghurst:** Writing – review & editing, Resources, Investigation. **Khaled M. Ibrahim:** Investigation. **Jamie H. Warner:** Resources, Investigation. **Chandra Veer Singh:** Writing – review & editing, Supervision, Software, Resources. **Zhongchao Tan:** Writing – review & editing. **Samira Siahrostami:** Writing – review & editing, Software. **Yimin A. Wu:** Writing – review & editing, Supervision, Resources, Funding acquisition, Conceptualization.

Declaration of competing interest

The authors declare that they have no known competing financial interests or personal relationships that could have appeared to influence the work reported in this paper.

Appendix A. Supplementary data

Supplementary data to this article can be found online at https://doi.org/10.1016/j.cej.2024.156728.

Data availability

The authors declare that all data supporting this study are available within the paper and Supplementary Information files. Source data are provided upon on request.

References

[1] A. Herzog, et al., Operando investigation of Ag-decorated Cu2O nanocube catalysts with enhanced CO2 electroreduction toward liquid products, Angew. Chem., Int. Ed. 60 (13) (2021) 7426–7435.

[2] S. Nitopi, et al., Progress and perspectives of electrochemical CO2 reduction on copper in aqueous electrolyte, Chem. Rev. 119 (12) (2019) 7610–7672.

[3] O.G. Sánchez, et al., Recent advances in industrial CO2 electroreduction, Curr. Opin. Green Sustain. Chem. 16 (2019) 47–56.

[4] L. Fan, et al., Strategies in catalysts and electrolyzer design for electrochemical CO2 reduction toward C2+ products, Sci. Adv. 6 (8) (2020) eaay3111.

[5] Y.i. Hori, Electrochemical CO 2 reduction on metal electrodes, Modern Aspects Electrochem. (2008,) 89–189.

[6] T.T. Hoang, et al., Nanoporous copper–silver alloys by additive-controlled electrodeposition for the selective electroreduction of CO2 to ethylene and ethanol, J. Am. Chem. Soc. 140 (17) (2018) 5791–5797.

[7] Z. Chang, et al., The tunable and highly selective reduction products on Ag@ Cu bimetallic catalysts toward CO2 electrochemical reduction reaction, J. Phys. Chem. C 121 (21) (2017) 11368–11379.

[8] Q. Lei, et al., Investigating the origin of enhanced C2+ selectivity in oxide-/hydroxide-derived copper electrodes during CO2 electroreduction, J. Am. Chem. Soc. 142 (9) (2020) 4213–4222.

[9] S.Y. Lee, et al., Mixed copper states in anodized Cu electrocatalyst for stable and selective ethylene production from CO2 reduction, J. Am. Chem. Soc. 140 (28) (2018) 8681–8689.

[10] Z. Chen, et al., Grain-boundary-rich copper for efficient solar-driven electrochemical CO2 reduction to ethylene and ethanol, J. Am. Chem. Soc. 142 (15) (2020) 6878–6883.

[11] J. Wang, et al., Grain-boundary-engineered La2CuO4 perovskite nanobamboos for efficient CO2 reduction reaction, Nano Lett. 21 (2) (2021) 980–987.

[12] A. Loiudice, et al., Tailoring copper nanocrystals towards C2 products in electrochemical CO2 reduction, Angew. Chem., Int. Ed. 55 (19) (2016) 5789–5792.

[13] M. Ma, et al., Controllable hydrocarbon formation from the electrochemical reduction of CO2 over Cu nanowire arrays, Angew. Chem., Int. Ed. 55 (23) (2016) 6680–6684.

[14] S. Ma, et al., Electroreduction of carbon dioxide to hydrocarbons using bimetallic Cu–Pd catalysts with different mixing patterns, J. Am. Chem. Soc. 139 (1) (2017) 47–50.

[15] Q. Lei, et al., Structural evolution and strain generation of derived-Cu catalysts during CO2 electroreduction, Nat. Commun. 13 (1) (2022) 4857.

[16] Z. Wu, et al., Grain boundary and interface interaction Co-regulation promotes SnO2 quantum dots for efficient CO2 reduction, Chem. Eng. J. 451 (2023) 138477.

[17] R.G. Mariano, et al., Selective increase in CO2 electroreduction activity at grain-boundary surface terminations, Science 358 (6367) (2017) 1187–1192.

[18] X. Feng, et al., A direct grain boundary-activity correlation for CO electroreduction on Cu nanoparticles, ACS Cent. Sci. 2 (3) (2016) 169–174.

[19] J. Van Muylder, Electrochemical Materials Science Ch. 1, Springer US, Boston, MA, 1981.

[20] W. Zhang, et al., Atypical oxygen-bearing copper boosts ethylene selectivity toward electrocatalytic CO2 reduction, J. Am. Chem. Soc. 142 (26) (2020) 11417–11427.

[21] Q. Zhu, et al., Carbon dioxide electroreduction to C2 products over copper-cuprous oxide derived from electrosynthesized copper complex, Nat. Commun. 10 (1) (2019) 3851.

[22] H. Mistry, et al., Highly selective plasma-activated copper catalysts for carbon dioxide reduction to ethylene, Nat. Commun. 7 (1) (2016) 1–9.

[23] S.H. Lee, et al., Oxidation state and surface reconstruction of Cu under CO2 reduction conditions from in situ X-ray characterization, J. Am. Chem. Soc. 143 (2) (2020) 588–592.

[24] Y. Yang, et al., Operando studies reveal active Cu nanograins for CO2 electroreduction, Nature 614 (7947) (2023) 262–269.

[25] C.W. Li, et al., Electroreduction of carbon monoxide to liquid fuel on oxide-derived nanocrystalline copper, Nature 508 (7497) (2014) 504–507.

[26] Y. Wang, et al., Defect and interface engineering for aqueous electrocatalytic CO2 reduction, Joule 2 (12) (2018) 2551–2582.

[27] V.P. Zhdanov, Simulations of oxidation of metal nanoparticles with a grain boundary inside, React. Kinet. Mech. Catal. 130 (2) (2020) 685–697.

[28] W.J. Dong, et al., Grain boundary engineering of Cu–Ag thin-film catalysts for selective (photo) electrochemical CO2 reduction to CO and CH4, ACS Appl. Mater. Interfaces. 13 (16) (2021) 18905–18913.

[29] H. Xiao, et al., Cu metal embedded in oxidized matrix catalyst to promote CO2 activation and CO dimerization for electrochemical reduction of CO2, PNAS 114 (26) (2017) 6685–6688.

[30] C.W. Lee, et al., Defining a materials database for the design of copper binary alloy catalysts for electrochemical CO2 conversion, Adv. Mater. 30 (42) (2018) 1704717.

[31] S. Stoll, A. Schweiger, EasySpin, a comprehensive software package for spectral simulation and analysis in EPR, J. Magn. Reson. 178 (1) (2006) 42–55.

[32] P.E. Blöchl, Projector augmented-wave method, Phys. Rev. B 50 (24) (1994) 17953.

[33] J.P. Perdew, et al., Generalized gradient approximation made simple, Phys. Rev. Lett. 77 (18) (1996) 3865.

[34] S. Grimme, Semiempirical GGA-type density functional constructed with a long-range dispersion correction, J. Comput. Chem. 27 (15) (2006) 1787–1799.

[35] J.K. Nørskov, et al., Origin of the overpotential for oxygen reduction at a fuel-cell cathode, J. Phys. Chem. B 108 (46) (2004) 17886–17892.

[36] C. Yang, et al., Overcoming immiscibility toward bimetallic catalyst library, Sci. Adv. 6 (17) (2020) eaaz6844.

[37] W.J. Dong, et al., Tailoring electronic structure of bifunctional Cu/Ag layered electrocatalysts for selective CO2 reduction to CO and CH4, Nano Energy 78 (2020) 105168.

[38] S. Mu, et al., Hydroxyl radicals dominate reoxidation of oxide-derived Cu in electrochemical CO2 reduction, Nat. Commun. 13 (1) (2022) 3694.

[39] L. Wang, et al., Stabilized Cuδ+-OH species on in situ reconstructed Cu nanoparticles for CO2-to-C2H4 conversion in neutral media, Nat. Commun. 15 (1) (2024) 7477.

[40] L. Wang, et al., Revealing real active sites in intricate grain boundaries assemblies on electroreduction of CO2 to C2+ products. Adv. Energy Mater., 2402636.

[41] X. Lv, et al., Electron-deficient Cu sites on Cu3Ag1 catalyst promoting CO2 electroreduction to alcohols, Adv. Energy Mater. 10 (37) (2020) 2001987.

[42] J.D. Yi, et al., Highly selective CO2 electroreduction to CH4 by in situ generated Cu2O single-type sites on a conductive MOF: stabilizing key intermediates with hydrogen bonding, Angew. Chem., Int. Ed. 59 (52) (2020) 23641–23648.

[43] X.-Y. Ma, et al., Electrolyte-layer-tunable ATR-SEIRAS for simultaneous detection of adsorbed and dissolved species in electrochemistry, Anal. Chem. 94 (32) (2022) 11337–11344.

[44] Y. Zhang, et al., In situ carbon-encapsulated copper-doped cerium oxide derived from MOFs for boosting CO2-to-CH4 electro-conversion, ACS Catal. 13 (2023) 1545–1553.

[45] X. Li, et al., Selective visible-light-driven photocatalytic CO2 reduction to CH4 mediated by atomically thin CuIn5S8 layers, Nat. Energy. 4 (8) (2019) 690–699.

[46] B. Zijlstra, et al., First-principles microkinetics simulations of electrochemical reduction of CO2 over Cu catalysts, Electrochim. Acta. 335 (2020) 135665.

[47] H. Zhang, et al., Computational and experimental demonstrations of one-pot tandem catalysis for electrochemical carbon dioxide reduction to methane, Nat. Commun. 10 (1) (2019) 3340.